ORIGINAL ARTICLE

*Journal of Cachexia, Sarcopenia and Muscle* 2019; **10**: 1128–1142
Published online 18 July 2019 in Wiley Online Library (wileyonlinelibrary.com) **DOI:** 10.1002/jcsm.12450

# Macrophages protect against loss of adipose tissue during cancer cachexia

Merve Erdem[1,2], Diana Möckel[3], Sandra Jumpertz[1], Cathleen John[4†], Athanassios Fragoulis[1], Ines Rudolph[5], Johanna Wulfmeier[1], Jochen Springer[4], Henrike Horn[6], Marco Koch[6], Georg Lurje[1,7,8], Twan Lammers[3,9,10], Steven Olde Damink[7,8,11], Gregory van der Kroft[1,7,8], Felix Gremse[3] & Thorsten Cramer[1,7,8,11,12]*

[1]*Department of General, Visceral and Transplantation Surgery, University Hospital RWTH Aachen, Aachen, Germany,* [2]*Berlin School of Integrative Oncology, Charité—Universitätsmedizin Berlin, Campus Virchow-Klinikum, Berlin, Germany,* [3]*Institute for Experimental Molecular Imaging, Center for Biohybrid Medical Systems, University Hospital RWTH Aachen, Aachen, Germany,* [4]*Department of Cardiology, Charité—Universitätsmedizin Berlin, Campus Virchow-Klinikum, Berlin, Germany,* [5]*Department of Hepatology and Gastroenterology, Charité—Universitätsmedizin Berlin, Campus Virchow-Klinikum, Berlin, Germany,* [6]*Institute of Anatomy, University of Leipzig, Leipzig, Germany,* [7]*ESCAM—European Surgery Center Aachen Maastricht, Aachen, Germany,* [8]*ESCAM—European Surgery Center Aachen Maastricht, Maastricht, The Netherlands,* [9]*Department of Targeted Therapeutics, MIRA Institute for Biomedical Technology and Technical Medicine, University of Twente, Enschede, The Netherlands,* [10]*Department of Pharmaceutics, Utrecht Institute for Pharmaceutical Sciences, Utrecht University, Utrecht, The Netherlands,* [11]*Department of Surgery, Maastricht University Medical Centre, Maastricht, The Netherlands,* [12]*NUTRIM School of Nutrition and Translational Research in Metabolism, Maastricht University, Maastricht, The Netherlands*

## Abstract

**Background** Cancer cachexia represents a central obstacle in medical oncology as it is associated with poor therapy response and reduced overall survival. Systemic inflammation is considered to be a key driver of cancer cachexia; however, clinical studies with anti-inflammatory drugs failed to show distinct cachexia-inhibiting effects. To address this contradiction, we investigated the functional importance of innate immune cells for hepatocellular carcinoma (HCC)-associated cachexia.

**Methods** A transgenic HCC mouse model was intercrossed with mice harbouring a defect in myeloid cell-mediated inflammation. Body composition of mice was analysed via nuclear magnetic resonance spectroscopy and microcomputed tomography. Quantitative PCR was used to determine adipose tissue browning and polarization of adipose tissue macrophages. The activation state of distinct areas of the hypothalamus was analysed via immunofluorescence. Multispectral immunofluorescence imaging and immunoblot were applied to characterize sympathetic neurons and macrophages in visceral adipose tissue. Quantification of pro-inflammatory cytokines in mouse serum was performed with a multiplex immunoassay. Visceral adipose tissue of HCC patients was quantified via the L3 index of computed tomography scans obtained during routine clinical care.

**Results** We identified robust cachexia in the HCC mouse model as evidenced by a marked loss of visceral fat and lean mass. Computed tomography-based analyses demonstrated that a subgroup of human HCC patients displays reduced visceral fat mass, complementing the murine data. While the myeloid cell-mediated inflammation defect resulted in reduced expression of pro-inflammatory cytokines in the serum of HCC-bearing mice, this unexpectedly did not translate into diminished but rather enhanced cachexia-associated fat loss. Defective myeloid cell-mediated inflammation was associated with decreased macrophage abundance in visceral adipose tissue, suggesting a role for local macrophages in the regulation of cancer-induced fat loss.

**Conclusions** Myeloid cell-mediated inflammation displays a rather unexpected beneficial function in a murine HCC model. These results demonstrate that immune cells are capable of protecting the host against cancer-induced tissue wasting, adding a further layer of complexity to the pathogenesis of cachexia and providing a potential explanation for the contradictory results of clinical studies with anti-inflammatory drugs.

**Keywords** Cancer-associated cachexia; Hepatocellular carcinoma; Visceral adipose tissue; Macrophages; HIF-1α

*Received: 14 November 2018; Revised: 1 March 2019; Accepted: 29 April 2019*
**Correspondence to: Thorsten Cramer, Molecular Tumor Biology, Department of General, Visceral and Transplantation Surgery, University Hospital RWTH Aachen, Pauwelsstraße 30, 52074 Aachen, Germany. Phone: +49 241 8036353, Fax: +49 241 8082068, Email:* tcramer@ukaachen.de
†*Present address: Department of Molecular Toxicology, German Institute of Human Nutrition Potsdam-Rehbrücke, Arthur-Scheunert-Allee 114-116, 14558 Nuthetal, Germany, and German Center for Cardiovascular Research (DZHK), 10117 Berlin, Germany.*

## Introduction

Cachexia is a multifactorial metabolic syndrome characterized by weight loss due to depletion of muscle with or without loss of fat.[1] Systemic inflammation, insulin resistance, enhanced muscle protein breakdown, and sympathetic nervous system activation are hallmarks of cachexia. A plethora of diseases are associated with cachexia, for example, chronic infections (HIV and tuberculosis), chronic heart failure, chronic obstructive lung disease, and chronic kidney failure.[2] The most common association, however, exists between cachexia and cancer, where it can occur in up to 80% of cases.[3] Cancer-associated cachexia (CAC) goes along with unfavourable prognosis and plays a causal role in up to 20% of cancer-related deaths.[3] CAC is unresponsive to nutritional support, and while a lot of progress has been made in the past years regarding the mechanisms of CAC, an effective treatment option is still missing.

Patients suffering from hepatocellular carcinoma (HCC) typically show loss of muscle mass and strength (termed sarcopenia), resulting in frailty and debilitating physical weakness.[4] In addition, cachexia is a common characteristic of HCC patients, which not only reduces the quality of life but also—together with sarcopenia—impacts significantly on overall prognosis[5] and clinical decision making: Mortality of HCC patients after intra-arterial therapy[6] and liver transplantation[7] as well as dose-limiting toxicities of sorafenib,[8] which is the gold standard oral treatment for non-resectable HCC, are independently predicted by sarcopenia. Taken together, cachexia and sarcopenia are of pivotal importance for both patients (quality of life and prognosis) and clinicians (progression and treatment decision).

Against this background, a better understanding of the molecular and cell biological mechanisms that govern HCC-associated sarcopenia and cachexia is urgently needed. As cachexia is a multifactorial syndrome affecting various organs and cellular systems, this can only be achieved by using *in vivo* model systems that recapitulate the syndrome as a whole.[9] With respect to HCC-associated cachexia, the most widely applied system is the rat ascites hepatoma Yoshida AH-130 model. This is characterized by a hypercatabolic state and marked depletion of both skeletal muscle and adipose tissue.[10,11] While the Yoshida AH-130 model is certainly of great value, especially for the identification of potential cachexia-inhibiting drugs,[12,13] a better understanding of the pathogenesis of HCC-associated cachexia is limited by the absence of a practicable murine model system. Intercrossing such a mouse model with conventional or cell type-specific knockout mice would enable researchers to address a number of hypotheses and would undoubtedly result in a much better understanding of the molecular and cell biological mechanisms that govern HCC-associated cachexia.[14]

Here, we describe a robust cachexia phenotype in a transgenic murine HCC model. Intercrosses with mice harbouring defective myeloid cell-mediated inflammation unexpectedly resulted in enhanced cachexia-associated loss of adipose tissue even though systemic levels of pro-inflammatory cytokines were lower in the knockout mice. Furthermore, we present experimental data arguing for a protective role of macrophages in the context of CAC-associated fat loss. Taken together, our results challenge the general understanding of pro-inflammatory cytokines as causal agents of CAC and establish a functional importance of macrophages in the setting of CAC-associated fat loss that has not been previously appreciated.

## Materials and methods

### Animals

Hepatocyte-specific expression of the SV40 large T oncoprotein in ASV-B mice was achieved by the antithrombin III promoter.[15] Only male mice develop tumours as the transgene is located on the Y chromosome. ASV-B mice (pure C57BL/6J background) were further crossed with mice with both alleles of *Hif1a* gene flanked by loxP sites at exon 2 (*Hif1a* $+^{f}/+^{f}$). Myeloid cell-specific knockout of *Hif1a* was achieved by breeding ASV-B male *Hif1a* $+^{f}/+^{f}$ mice with female *Hif1a* $+^{f}/+^{f}$ mice expressing Cre recombinase driven by the lysozyme M promoter. In our study, we used male ASV-B/*Hif1a* $+^{f}/+^{f}$ mice, additionally positive for Cre expression (ASV-B/LysCre+/*Hif1a* $+^{f}/+^{f}$), as knockouts (named ASV-B Hif1a$^{MC}$) and Cre-negative littermates as wild type (WT). C57BL/6J male mice were used as controls. All animals were maintained in a specific pathogen-free facility. Mice were given water and standard rodent chow *ad libitum* and were kept at constant room temperature with a 12 h light/dark cycle. All experiments were approved by local authorities (LAGESO Berlin and LANUV Recklinghausen, Germany) and conducted in accordance with the national and institutional guidelines for care, welfare, and treatment for animals.

### Organ harvest

ASV-B mice were sacrificed at the age of 12, 16, and 18 weeks. Sixteen-week-old C57BL/6J male mice were used as control for tissue weights. Blood serum, liver, epididymal white adipose tissue (eWAT), skeletal muscle (gastrocnemius, soleus, tibialis anterior, and extensor digitorum longus), and heart were collected and weighed after sacrifice.

## Body weight and composition

Chow and water were quantified in each cage on the first and the last day of each week, and consumed amounts were calculated and expressed per week. Body weight was measured once per week. Body composition was analysed via nuclear magnetic resonance (NMR) spectroscopy device EchoMRI-700™ (Echo Medical Systems, Houston, TX, USA) once a week to measure total body fat and lean mass.

## In vivo microcomputed tomography imaging

*In vivo* microcomputed tomography (μCT) imaging of normal C57BL/6, ASV-B WT, and ASV-B Hif1a$^{MC}$ mice was performed using a dual-energy gantry-based flat-panel μCT scanner (TomoScope 30s Duo, CT Imaging, Erlangen, Germany). The dual-energy X-ray tubes of the μCT were operated at voltages of 40 and 65 kV with currents of 1.0 and 0.5 mA, respectively. To cover the entire mouse, three sub-scans were performed, each of which acquired 720 projections with 1032 × 1012 pixels during one full rotation with durations of 90 s. Animals were sacrificed just before imaging. After acquisition, volumetric data sets were reconstructed using a modified Feldkamp algorithm with a smooth kernel at an isotropic voxel size of 35 μm. The fat-containing tissue regions, which appear hypo-intense in the μCT data, were segmented using an automated segmentation method with interactive correction of segmentation errors.[16] The volumetric fat percentage was computed as the ratio of (subcutaneous and visceral) fat volume to the entire body volume.

## RNA isolation and quantitative PCR

Total RNA from snap-frozen eWAT of 16-week-old animals was isolated using NucleoZOL (Macherey Nagel, Düren, Germany), and reverse transcription was performed using Maxima Reverse Transcriptase together with Oligo (dT)18 Primers, Random Hexamer Primers, and dNTP Mix (Thermo Fisher Scientific, Langerwehe, Germany). Quantitative real-time PCR was performed using Applied Biosystems 7500 Real-Time PCR System in 96-well format, each reaction containing 15 ng cDNA, 0.3 μM specific primer, and 1× *Power* SYBR Green Master Mix reagent (Applied Biosystems, Bleiswijk, The Netherlands). Primers for *Ucp1*, *Pgc1a*, *Pparg*, *Prdm16*, *Cidea*, and *Mrc1* were chosen from published literature.[17,18] Primers against *B2m* (F: 5′-TTCTGGTGCTTGTCTCACTGA-3′, R: 5′-CAGTATGTTCGGCTTCCCATTC-3′), *Arg1* (F: 5′-CTCCAAGCCAAAGTCCTTAGAG-3′, R: 5′-AGGAGCTGTCATTAGGGACATC-3′), *Clec10a* (F: 5′-GGCACAAAACCCAGCAAGAC-3′, R: 5′-TGGGACCAAGGAGAGTGCTA-3′), *Il10* (F: 5′-GCTCTTACTGACTGGCATGAG-3′, R: 5′-CGCAGCTCTAGGAGCATGTG-3′), *Tnfa* (F: 5′-CCATTCCTGAGTTCTGCAAAGG-3′, R: 5′-AGGTAGGAAGGCCTGAGATCTTATC-3′), *Azgp1* (F: 5′-ACACTACAGGGTCTCACACCT-3′, R: 5′-TCGCTGCACGTAGACCTTTT-3′), *Lipe* (F: 5′-TGTCACGCTACACAAAGGCT-3′, R: 5′-GGTCACACTGAGGCCTGTC-3′), and *Hif1a* (F: 5′-GCTTCTGTTATGAGGCTCACC-3′, R: 5′-ATGTCGCCGTCATCTGTTAG-3′) were selected to span exon borders and were validated according to the MIQE guidelines.[19] Relative mRNA expressions were calculated using the comparative delta-CT method and normalized to *B2m*.

## Cytokine measurement

Blood was collected from sacrificed mice via inferior vena cava using a 22 G needle and transferred to serum-gel Z tubes (Sarstedt, Germany), allowed to clot for 30 min at room temperature and centrifuged at 10 000 *g* for 5 min. The serum was collected and stored frozen until use. To detect interleukin-1 beta (Il-1β), interleukin-6 (Il-6), and tumour necrosis factor-alpha (Tnf-α) simultaneously, Bio-Plex Pro™ mouse cytokine Th17 panel A 6-Plex kit (Bio-Rad, Germany) was used according to the manufacturer's instructions. Samples were diluted at 1:2, and the fluorescence measurement of the beads was performed with the Qiagen LiquiChip 200 workstation (Hilden, Germany). Cytokine concentrations were calculated using Bio-Plex Manager software (Bio-Rad, Hercules, CA, USA).

## Immunohistochemistry and tissue analysis

Mice were sacrificed, and tissues were fixed in 10% formalin overnight, followed by dehydration and embedding in paraffin. For histopathological evaluation, 2-μm-thick eWAT or liver sections were stained with haematoxylin and eosin. For adipose tissue, pictures of representative areas from each section in ×200 magnification were taken, and Adiposoft software was used to calculate cell size of 35 images per group in total. Minimal 20 μm and maximum 100 μm thresholds were set for automated measurement of adipocyte diameter followed by manual correction. A frequency distribution was calculated for each group. Total adipocyte number within the distribution was subsequently calculated, and the frequency was converted to a percentage of total adipocytes counted. For analyses of tumour areas, haematoxylin and eosin stained sections of ASV-B livers were used. Two tissue sections per mouse were used for evaluation. Images were taken using Axiocam 506 mono (Carl Zeiss), and tumour areas were quantified by ImageJ.

## Immunohistochemistry of murine hypothalamus

Free-floating coronal brain sections of 40 μm thickness were cut on a microtome (Leica VT1200) and stored in 0.02 M

PBS + 0.09% sodium azide until staining. For c-Fos immunolabelling, we used a modified version of a published protocol.[20] Slices containing the arcuate nucleus (ARC) were blocked and permeabilized in 0.02 M PBS + 0.3% Triton X-100 + 5% normal goat serum (NGS, Jackson ImmunoResearch) for 60 min. The slices were incubated in rabbit polyclonal anti-cfos-antibody (1:10 000, Synaptic Systems, #226003) in PBS + 0.3% Triton X-100 + 3% NGS for five nights at 4°C. After three washes in PBS + 0.3% Triton, brains were incubated with goat secondary antibodies raised against rabbit, conjugated to Alexa Fluor 488 (1:500, Invitrogen, #A11034) in PBS + 0.3% Triton X-100 + 3% NGS for 60–90 min at room temperature. To visualize nuclei, 4′,6-diamidin-2-phenylindol (DAPI, 1:10 000) was added for 5 min to one of the final three washing steps in PBS. Sections were mounted on glass slides (Menzel Gläser), embedded in fluorescence mounting medium (Dako), and covered with glass cover slips (Menzel Gläser). Brain sections were imaged using confocal laser scanning microscopy (Zeiss, LSM700), operated by ZEN 2011 SP3 (Zeiss). Images were taken using a 20× Plan-Neofluar objective (NA 0.5) using the same imaging parameters for all images. Optical sections (thickness: 9.8 μm in 488 channel, 9.9 μm in DAPI channel) were acquired in 5 μm steps from each hemisphere of the ARC. All image analysis was carried out in ImageJ (https://imagej.net) using custom macros. One optical section located in the middle of each brain slice was extracted, and brightness and contrast were adjusted with the same parameters for all images to improve visibility. Putative c-Fos positive cells were counted manually in the Alexa 488 channel using the Cell Counter plugin (https://imagej.net/Cell_Counter) by an observer blind to the experimental groups. Data from two staining experiments were taken together, and least four ARC hemispheres from two to three brain sections were analysed per animal.

## Triglyceride measurement

Blood samples were collected from sacrificed animals as described for cytokine measurements. The mice were fed *ad libitum*; blood samples were collected during the day, followed by serum separation. Triglycerides in serum samples were measured in the central biochemistry laboratory of the Institute for Laboratory Animal Science, University Hospital RWTH Aachen.

## Ex vivo lipolysis

Gonadal fat pads were excised from mice, cut into 20 mg pieces, and incubated at 37°C in Krebs–Ringer solution pH 7.4, containing 12 mM HEPES, 4.9 mM KCl, 121 mM NaCl, 1.2 mM $MgSO_4$, 0.33 mM $CaCl_2$, 3.5% (w/v) fatty acid-free BSA, and 0.1% (w/v) glucose. No stimulation was performed. Released glycerol was measured from supernatants after 4 h incubation using the Glycerol Colorimetric Assay Kit (Cayman), and tissue weights were used for normalization.

## Isolation and stimulation of bone marrow-derived macrophages

Bone marrow was collected from tibiae and femurs of 8- to 11-week-old WT and $Hif1a^{MC}$ mice. Red blood cells were lysed with ACK buffer in flushed marrows, and cells were seeded on cell culture plates in Roswell Park Memorial Institute (RPMI) supplemented with 10% fetal bovine serum (FBS), 100 U/mL penicillin, and 100 μg/mL streptomycin. After overnight incubation, non-attached cells were collected and cultured in RPMI supplemented with 20% FBS and 30% L929-conditioned medium for 1 week. Differentiated bone marrow-derived macrophages (BMDMs) were stimulated for 48 h with lipopolysaccharide (LPS) (100 ng/mL, Sigma Aldrich) and interferon (IFN)-γ (20 ng/mL) for classical activation and with IL-4 (20 ng/mL, both from eBioscience) for alternative activation of macrophages. Media were collected from polarized macrophages and used for catecholamine measurement.

## Catecholamine measurement

Catecholamine amounts were measured with high-performance liquid chromatography (HPLC). Snap-frozen eWAT samples were thawed and sonicated in 0.3 M perchloric acid for 30 s on ice (200 μL/0.1 g tissue). Samples were centrifuged at 7600 g for 10 min at 1°C. Supernatants, cleaned from residue, were collected and used for HPLC measurements. Cell culture media collected from BMDMs were directly injected into the system. All measurements were performed by a service laboratory with special expertise in HPLC (Laboratory for Stress Monitoring, Hardegsen, Germany).

## Western blotting

Fifty milligrams of eWAT samples were homogenized in 100 μL RIPA buffer containing 10 mM Tris–HCl (pH 7.5), 150 mM NaCl, 0.25% sodium dodecyl sulfate (SDS), 1% sodium deoxycholate, 1% NP40, 2 mM phenylmethylsulfonylfluorid (PMSF), 1 mM dithiothreitol (DTT), 10 mM NaF, 1 mM $Na_3O_4$ and 2 μM leupeptin, and $4.4 \times 10^{-4}$ TIU/mg aprotinin. After sonication, the homogenates were centrifuged for 15 min at 12 000 *g* at 4°C, and supernatants were collected. Total protein content was measured by Lowry assay (DC Protein Assay, Bio-Rad). Forty micrograms of protein were separated via SDS-polyacrylamide gel electrophoresis (PAGE) and transferred to a nitrocellulose membrane. The membrane was incubated overnight with

tyrosine hydroxylase (TH) antibody (Millipore, AB152) in 5% milk to 0.05% TBS-Tween 20 (1:1000), and β-actin antibody (Sigma, A5441) (1:5000) was used as a loading control. Membranes were developed using enhanced chemiluminescence reagent (PerkinElmer, Life Sciences) and visualized by ChemoCam Imager (INTAS, Göttingen, Germany).

### *Immunofluorescence staining and quantification*

Paraffin sections from eWAT with a thickness of 2 μm were deparaffinized and rehydrated according to standard protocols. Sections were re-fixed by 10 min incubation in 3.5% formalin, and antigen retrieval was performed by 15 min of cooking at 110°C in Dako target retrieval solution in the Decloaking Chamber (Biocare Medical, Berlin, Germany). After 10 min of blocking in Dako antibody diluent, sections were incubated with F4/80 (eBioscience #14–4801) antibody in a 1:2000 dilution for 30 min followed by ImmPRESS anti-rat IgG (Vector) incubation for 20 min. For permanent labelling of F4/80 with a fluorescent tag, sections were treated with Opal 570 (Opal 4-colour IHC kit, PerkinElmer, 1:50 in amplification reagent) for 10 min. Subsequently, the antibodies were detached from sections by microwave cooking in AR6 buffer (Opal 4-colour IHC kit, PerkinElmer), whereas the Opal fluorophore remained fixed to the tissue. For staining of a second marker, sections were directly processed further, and the described procedure was repeated. Briefly, sections were blocked again and incubated with anti-TH (Millipore #AB152, 1:5000), anti-Ki-67 (Cell Signaling #12202, 1:3000), or anti-Ym-1 (Stemcell Tech. #60130, 1:5000). Following anti-rabbit IgG treatment, antigens were labelled with Opal 520 (Opal 4-colour IHC kit, PerkinElmer, 1:100 in amplification reagent). After microwave treatment, nuclei were stained with spectral DAPI (PerkinElmer) for 5 min. Tissue sections were covered with Vectashield HardSet antifade mounting medium (Vector Laboratories). Fluorescent signals were detected, separated, and recorded using the Vectra 3.0 multiplex imaging system (PerkinElmer). Quantification of signals was performed via inForm automated image analysis software (PerkinElmer).

### *L3 visceral adipose tissue index analysis of HCC patients*

Computed tomography scans (performed maximally 6 weeks before surgery) obtained from routine clinical work from 63 HCC patients without liver cirrhosis of the Department of General, Transplantation, and Visceral Surgery at the University Hospital RWTH Aachen were scheduled for body composition analysis following ethics approval of the local authorities. Patients' age ranged from 21 to 86 years (mean 68), 45% were female and 55% male, body mass index ranged from 17.7 to 36.3 kg/m$^2$ (mean 26), and T stage was 34% T1, 30% T2, 26% T3, and 10% T4. CT scans were selected and analysed by a single investigator in a blinded approach and anonymized format using Slice-O-matic software, version 5.0 (Tomovision, Montreal, QC, Canada). The third lumbar vertebra (L3) was used as a standard landmark to measure tissue cross-sectional area in cm$^2$ as previously reported.[21] In short, visceral adipose tissue (VAT) was identified and quantified on CT images using predefined Hounsfield unit ranges (−150 to −50 Hounsfield unit). Values were corrected for height to calculate the L3 VAT index in cm$^2$/m$^2$, providing good estimates of total body VAT mass.[21] We considered our cohort too small for cut-point analysis by optimal stratification and therefore determined cut-off values based on tertiles stratified by sex. Determining the cut-off at a tertile enables comparison between groups with a relatively low/high value to be compared with the rest of the group while not forcing subjects with a value around the cut-off value in a low or high category.[22] Cut-off values were set at the lowest tertile for all body composition variables. Twenty-two cases were excluded due to no CT scan being available ($n$ = 10), bad quality of the CT scan ($n$ = 5), and L3 not being visible on the scan ($n$ = 7). Consequently, 41 patients became eligible for analysis. The study was approved by the local ethics committee (EK 343/15) and was conducted in accordance to the principles of the Declaration of Helsinki and 'good clinical practice' guidelines.

### *Statistical analysis*

The statistical analyses of animal data were carried out with Student's $t$-test or by one-way analysis of variance, followed by appropriate corrections or post hoc tests as indicated in the figure legends. Statistical analyses were carried out with GraphPad Prism 6 software (GraphPad, CA, USA). Patient data were analyzed with Fisher's exact test in SPSSv25 (IBM, New York, USA) software. Data are presented as mean and standard error of the mean (SEM), and the asterisks in the graphs indicate statistically significant changes with $P$ values: $^{*}P < 0.05$, $^{**}P < 0.01$, and $^{***}P < 0.001$.

## Results

### *ASV-B mice display robust cancer-associated cachexia*

The transgenic ASV-B mouse line is a well-established HCC model based on hepatocyte-specific expression of the SV40 large T oncogene.[15] In this model, mice develop dysplastic hepatocytes at 8, hepatic adenomas at 12, and HCCs at 16 weeks of age.[23] We initially evaluated the HCC progression by measuring liver weight in different age groups. As shown in *Figure* 1A, liver weight of ASV-B mice strongly increased with age compared with tumour-free C57BL/6J controls

(16 weeks old), reflecting tumour progression. Rather unexpectedly, this pronounced increase of liver mass did not affect total body weight. In fact, ASV-B mice were even slightly lighter than tumour-free C57BL/6J mice between 12 and 18 weeks of age (*Figure* 1B). Food and water intake were not different between control and HCC-bearing mice, ruling out a functional relevance of anorexia in this setting (*Figure* 1C). Altogether, the observed phenotype led us to consider tissue wasting and cachexia in the course of ASV-B tumour formation. To address this, we initially evaluated the mass of different skeletal muscle regions. As can be seen in *Figure* 1D, tumour-bearing mice showed a significant decrease in mass of gastrocnemius, tibialis anterior, and extensor digitorum longus muscle over time. Furthermore, heart weight was diminished in ASV-B compared with tumour-free mice in all age groups (*Figure* 1D). Along with the muscle wasting, we observed a striking loss of adipose tissue in tumour-bearing mice. Measurement of gonadal fat depots revealed that fat loss started at 12 weeks of age and continued throughout tumour progression (*Figure* 1E). A representative image of an ASV-B mouse at the age of 16 weeks shows visibly smaller gonadal fat depots and clear tumour nodules in the massively enlarged liver (*Figure* 1F). The loss of adipose tissue and muscle mass illustrates the development of CAC in ASV-B mice.

## *Defective myeloid cell-mediated inflammation unexpectedly aggravates loss of adipose tissue in hepatocellular carcinoma-bearing mice*

Systemic inflammation is widely appreciated as a driving force of cachexia.[24] Myeloid cells, for example, granulocytes, monocytes, and macrophages, are the chief cellular effectors of the innate immune system and centrally involved in cancer-associated inflammation.[25] Earlier work by us and others has identified the hypoxia-inducible transcription factor HIF-1 as an essential regulator of myeloid cell-mediated inflammation.[26] We sought to investigate the functional importance of myeloid cells for the pathogenesis of CAC in ASV-B mice. To this end, we intercrossed ASV-B mice with myeloid cell-specific *Hif1a* knockout mice (termed ASV-B/Hif1a$^{MC}$, knockout efficiency is shown in Supporting Information, *Figure* S1) and analysed body weight and body composition. As can be seen in *Figure* 2A, ASV-B/Hif1a$^{MC}$ mice displayed a non-significant tendency for higher body weight than WT mice (termed ASV-B WT). Body composition analysis by NMR spectroscopy showed a lower amount of total body fat in ASV-B/Hif1a$^{MC}$ mice, again without reaching statistical significance (*Figure* 2B). In addition to NMR analyses, *in vivo* μCT imaging of mice was performed to visualize and quantify body composition. Two-dimensional cross-sectional images and three-dimensional volume renderings of segmented bones, lungs, liver, and fat were obtained. In *Figure* 2C, representative μCT images display fat loss in all depots as well as liver enlargement in tumour-bearing mice. Quantification of the volume analysis indicated a significant decrease of fat amount in ASV-B mice compared with controls (*Figure* 2D). The total fat amount in ASV-B/Hif1a$^{MC}$ mice tended to be lower than in ASV-B WT mice (significance level of 0.05, *Figure* 2D), which is consistent with the obtained NMR body composition results. Of note, skeletal muscle and heart weight did not differ between ASV-B WT and ASV-B/Hif1a$^{MC}$ mice (*Figure* S2). Taken together, the defective myeloid cell-mediated inflammation did not result in reduced CAC but unexpectedly aggravated the CAC-associated fat loss.

## *Visceral adipose tissue of ASV-B mice displays typical cachexia-associated changes*

We sought to identify the mechanisms underlying the loss of VAT in ASV-B mice and addressed the hypothesis that enhanced lipid mobilization takes place in HCC-bearing mice.[27,28] To this end, we quantified the cell size of adipocytes in eWAT and could show substantial cell shrinking between control and ASV-B mice (*Figure* 3A). ASV-B/Hif1a$^{MC}$ mice had a higher frequency of smaller adipocytes ($<$1500 $\mu m^2$) and lower frequency of larger adipocytes (1500–4000 $\mu m^2$) than ASV-B WT mice (statistically significant at 2000 $\mu m^2$) (*Figure* S3). It recently became clear that white adipose tissue (WAT) is able to switch to a thermogenic fat-burning phenotype (termed 'browning').[29] This process was found to contribute to the increased energy expenditure typical for cachexia in different mouse models of cancer cachexia.[18,29] We found significantly elevated mRNA levels of various browning marker genes in WAT of ASV-B mice in comparison with tumour-free controls (*Figure* 3B), demonstrating WAT browning in this HCC model. Of note, myeloid cell-specific deletion of *Hif1a* did not impact on browning marker gene expression in WAT (*Figure* 3B). Next, we focused on lipolysis of adipose tissue and performed an *ex vivo* lipolysis assay from eWAT. This assay allowed us to measure the secretion of glycerol from eWAT explants and demonstrated that ASV-B/Hif1a$^{MC}$ mice mobilize fat more efficiently than ASV-B WT mice (*Figure* 3C). Finally, we checked whether serum levels of triglycerides were increased. Here, under *ad libitum* food intake conditions, triglyceride levels were found elevated in ASV-B mice compared with controls. However, ASV-B WT and Hif1a$^{MC}$ mice exhibited similar triglyceride levels (*Figure* 3D).

## *Neither tumour load, pro-inflammatory cytokine expression, nor hypothalamic activation underlie the enhanced fat loss in ASV-B/Hif1a$^{MC}$ mice*

Having confirmed the unexpected aggravation of cancer-associated VAT loss in ASV-B/Hif1a$^{MC}$ mice, we next sought

**Figure 1** Characterization of cachexia in ASV-B mice. *(A)* Liver weight and *(B)* total body weight of C57BL/6 and ASV-B mice ($n$ = 8 per group) were measured at the indicated time points. *(C)* Food and water intake were measured weekly from 8 to 18 weeks of age in control ($n$ = 3) and ASV-B ($n$ = 8) mice. *(D)* Different muscle parts (GC, gastrocnemius; TA, tibialis anterior; EDL, extensor digitorum longus) were dissected and weighed for C57BL/6 mice ($n$ = 3) and ASV-B mice at the indicated time points ($n$ = 8, 5, and 4 in 12, 16, and 18 weeks, respectively). *(E)* The gonadal fat pad was removed and measured at ($n$ = 8 per group) at the same time points used in *(D)*. Data represent means with SEM. $^{*}P < 0.05$; $^{**}P < 0.01$; $^{***}P < 0.001$ according to two-way analysis of variance *(A)*, one-way analysis of variance followed by Tukey post hoc test *(B, D, E)*, or unpaired Student's $t$-test *(C)*. Panel *(F)* shows a general view of the abdominal cavity (above) and the resected livers (below) of control and ASV-B mice at the 16 week time point.

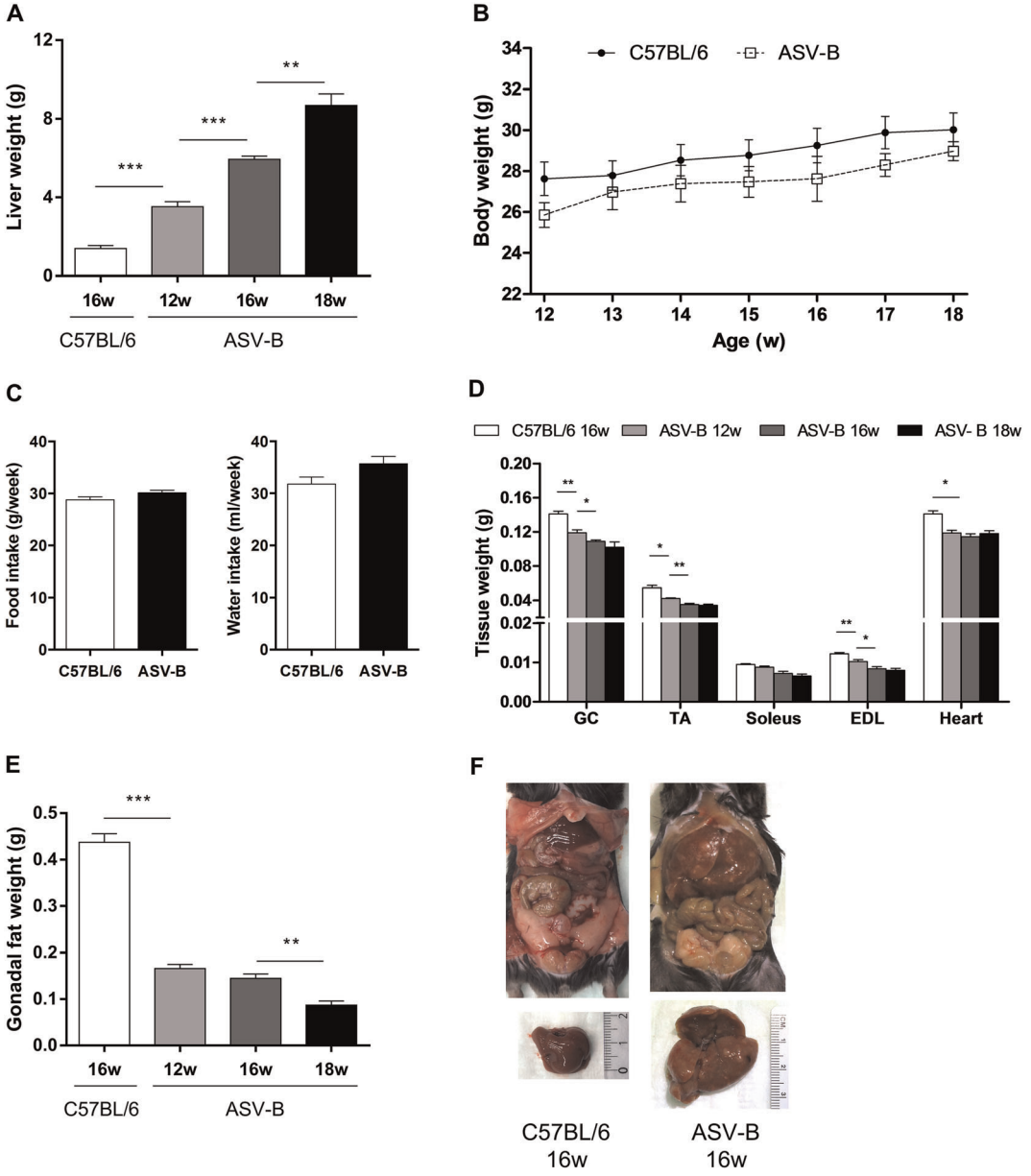


to identify the underlying mechanism(s). One obvious explanation would be an effect of the myeloid cell-specific *Hif1a* deletion on HCC formation, as we have observed for intestinal tumours.[30] However, neither μCT-based quantification of liver volume (*Figure* 4A), gross liver weight, nor histology-based measurements of tumour load (*Figure* 4B) displayed a difference between WT and ASV-B/Hif1a$^{MC}$ mice. As the hypothalamus is able to control lipid uptake and mobilization in WAT,[31] we analysed the activation state of neurons in the nucleus arcuatus (ARC) of the hypothalamus.[32] *Figure* 4C shows the number of c-Fos positive (+) cells in the ARC, reflecting the level of recent neuronal activation. The


DOI: 10.1002/jcsm.12450

**Figure 2** Myeloid cell-specific *Hif1a* knockout mice show aggravated fat loss in ASV-B mice. *(A)* Body weight of ASV-B wild type (WT) ($n$ = 8) and Hif1a$^{MC}$ ($n$ = 6) mice over time. *(B)* Weekly follow-up nuclear magnetic resonance analysis ($n$ = 7 per group) for body fat quantification. *(C)* Microcomputed tomography (μCT) imaging at 14-week-old C57BL/6, ASV-B WT, and ASV-B/Hif1a$^{MC}$ mice; upper panel shows representative two-dimensional cross-sectional μCT images in transversal planes of the abdomen of one representative mouse from each group (subcutaneous and visceral fat tissue is indicated in blue and green, respectively). Lower panel, representative images of three-dimensional volume renderings of segmented bones (white), lungs (pink), liver (brown), and fat (blue/green) upon *in vivo* μCT imaging, scale bar 1 cm. *(D)* Quantification of fat volume via μCT imaging ($n$ = 3 per group). Data show means with SEM. $^{*}P < 0.05$; $^{**}P < 0.01$; $^{***}P < 0.001$ according to two-way analysis of variance *(A, B)* and one-way analysis of variance followed by Tukey post hoc test *(D)*.

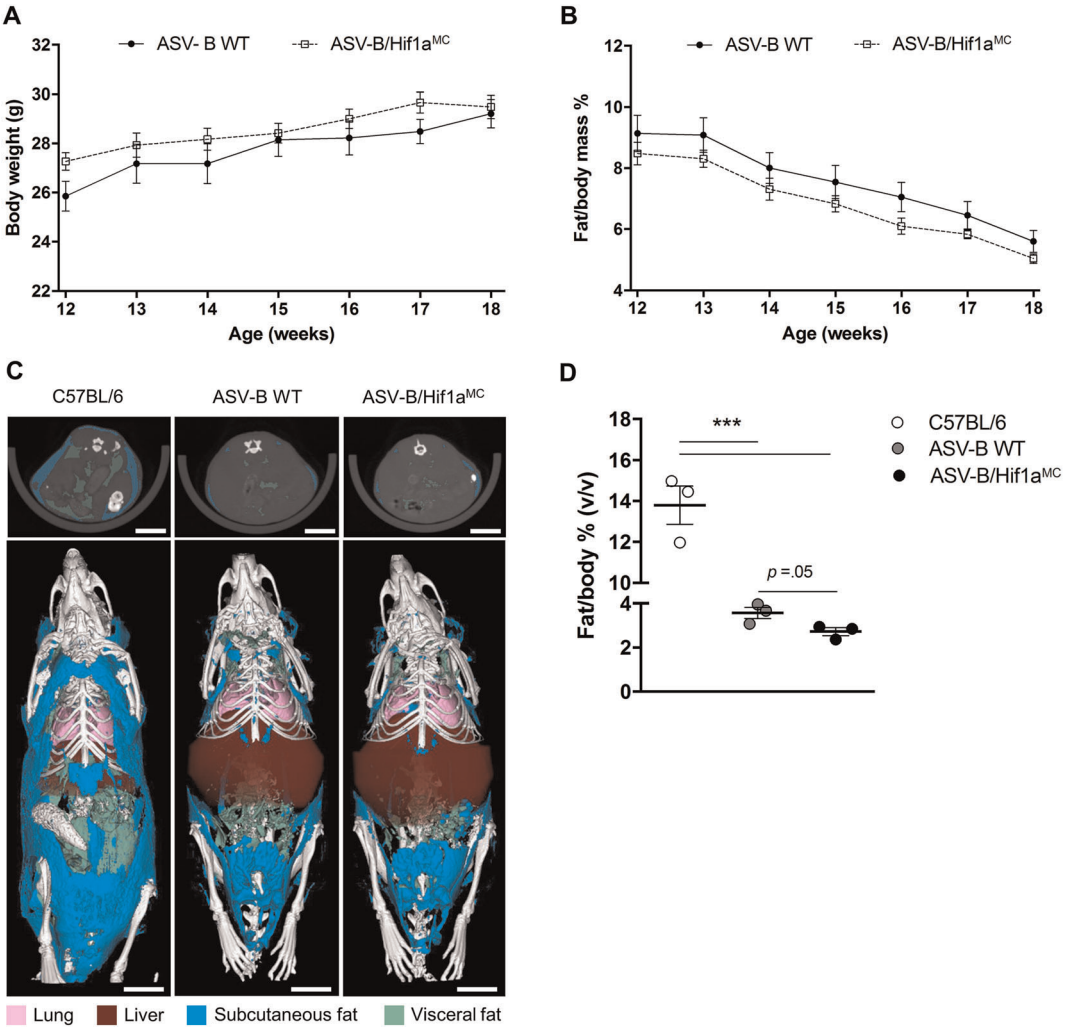


numbers of c-Fos+ cells in HCC-bearing mice are significantly increased, arguing for an elevated activation of the ARC. As the sympathetic nervous system has been shown to mediate the effects of the hypothalamus on WAT,[33] we measured catecholamine levels in peripheral fat tissue and found a significant increase in ASV-B compared with tumour-free mice (results for noradrenaline shown in *Figure* 4D, adrenaline was not detectable). Again, myeloid cell-specific *Hif1a* deletion remained without a significant effect in these experiments. In adipose tissue, macrophages were suggested as an alternative source of catecholamines,[17] although contradictory findings were published in later reports.[34] Of note, we were not able to detect noradrenaline or adrenaline in supernatants from BMDMs from WT and Hif1a$^{MC}$ mice, arguing that macrophages are not a likely source for catecholamines in adipose tissue. Next, we stained eWAT for TH, a marker of sympathetic neurons, the cells that synthesize catecholamines in their axons. Quantitative differences were observed neither between control and ASV-B mice nor between ASV-B WT and Hif1a$^{MC}$ mice (*Figure* 4E and 4F). Finally, we determined serum levels of pro-inflammatory cytokines, which have been shown in numerous studies to be positively associated with cachexia.[35,36] TNF-α, IL-6, and IL-1β are the best studied pro-inflammatory cytokines among

**Figure 3** Lipolysis and browning occur in adipose tissue of ASV-B mice. *(A)* Adipocyte cell size analysis in 16-week-old C57BL/6 ($n$ = 5), ASV-B wild type (WT) ($n$ = 4), and ASV-B/Hif1a$^{MC}$ ($n$ = 4) mice. Representative haematoxylin and eosin images of epididymal white adipose tissue (eWAT) of 16-week-old mice (right side), scale bars 50 μm. *(B)* mRNA levels of browning marker genes (*Ucp1*, *Ppargc1a*, *Pparg*, *Prdm16*, and *Cidea*) as determined by quantitative PCR in eWAT of 16-week-old C57BL/6 ($n$ = 3), ASV-B WT ($n$ = 3), and ASV-B/Hif1a$^{MC}$ ($n$ = 4) mice. *(C)* Glycerol release from eWAT of 16-week-old C57BL/6 ($n$ = 4), ASV-B WT ($n$ = 3), and ASV-B/Hif1a$^{MC}$ ($n$ = 3) mice as measured via *ex vivo* lipolysis assay for 2 h. *(D)* Triglyceride levels in serum of C57BL/6 ($n$ = 3), ASV-B WT ($n$ = 9), and ASV-B/Hif1a$^{MC}$ ($n$ = 9) mice. Data show means with SEM. $^{*}P < 0.05$; $^{**}P < 0.01$; $^{***}P < 0.001$ according to one-way analysis of variance followed by Tukey post hoc test.

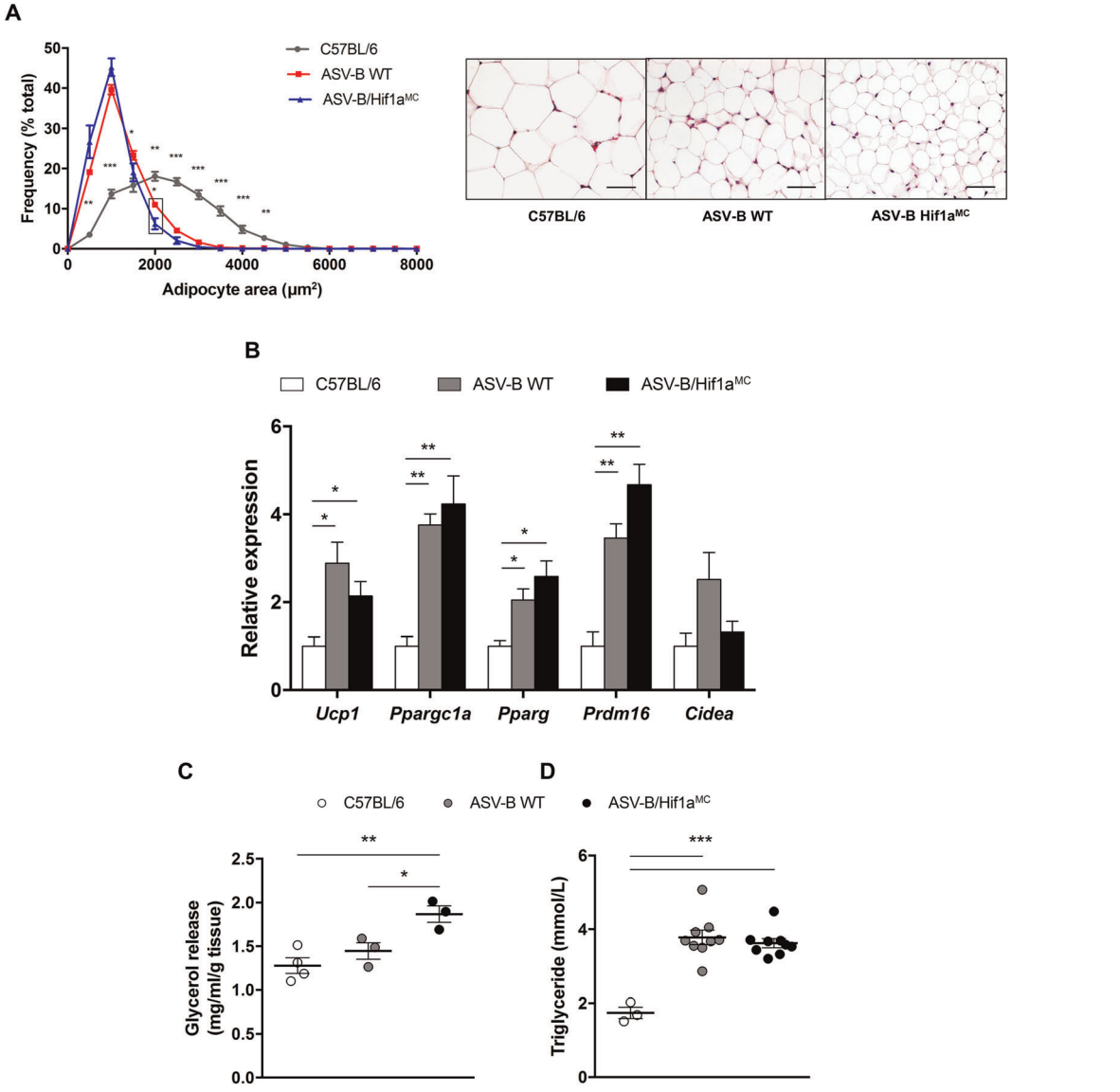


these, and they can be secreted by macrophages.[24] ASV-B WT mice showed significantly increased serum levels of Il-6, Il-1β, and Tnf-α compared with tumour-free control mice (*Figure* 4G). What is more, serum levels of Il-1β were significantly reduced, while IL-6 and TNF-α showed a tendency for decrease in ASV-B/Hif1a$^{MC}$ mice. Collectively, these results suggest a functional interplay of pro-inflammatory cytokines and the hypothalamus-peripheral sympathetic nervous system axis in regulating tumour-associated lipolysis in ASV-B mice.

## *Abundance of adipose tissue macrophages is controlled by Hif1a*

Macrophages have been shown to be important for adipose tissue homeostasis and can be recruited to and accumulate in adipose tissue after lipolysis, where they take part in local lipid regulation.[37] Against this background, we characterized different biological aspects of adipose tissue macrophages (ATM) in ASV-B mice. As it was shown that alternatively

**Figure 4** Analysis of potential mechanisms for enhanced fat loss in ASV-B/Hif1a$^{MC}$ mice. *(A)* Liver volume calculation using microcomputed tomography images ($n$ = 3 per group). *(B)* Livers were weighed at indicated time points ($n$ = 7, 4, and 4 at 12, 16, and 18 weeks, respectively), and tumour area assessment was performed at 16-week-old ASV-B wild type (WT) and Hif1a$^{MC}$ mice ($n$ = 3 per group). *(C)* Number of c-Fos+ cells in arcuate nucleus (ARC) of the hypothalamus of C57BL/6 ($n$ = 2), ASV-B WT ($n$ = 5), and ASV-B/Hif1a$^{MC}$ ($n$ = 3) mice at 16 weeks of age. *(D)* Noradrenalin levels in epididymal white adipose tissue (eWAT) of 16-week-old C57BL/6 ($n$ = 3), ASV-B WT ($n$ = 5), and ASV-B/Hif1a$^{MC}$ ($n$ = 4) mice. *(E)* (left) Representative images of immunofluorescence staining of tyrosine hydroxylase (TH) in eWAT from C57BL/6 ($n$ = 5), ASV-B WT ($n$ = 4), and ASV-B/Hif1a$^{MC}$ ($n$ = 5) mice, scale bars 50 μm; (right) quantification of staining, stained cells calculated as relative percentage of all counted cells. *(F)* Western blot of TH in eWAT from 16 weeks old ASV-B mice. *(G)* Serum inflammatory cytokine levels in control ($n$ = 8), ASV-B WT ($n$ = 11), and Hif1a$^{MC}$ ($n$ = 8) mice. Data show means with SEM. $^{*}P < 0.05$; $^{**}P < 0.01$; $^{***}P < 0.001$ according to one-way analysis of variance followed by Tukey post hoc test *(A, B, C, D, E, G)* and unpaired Student's $t$-test *(B, F)*.

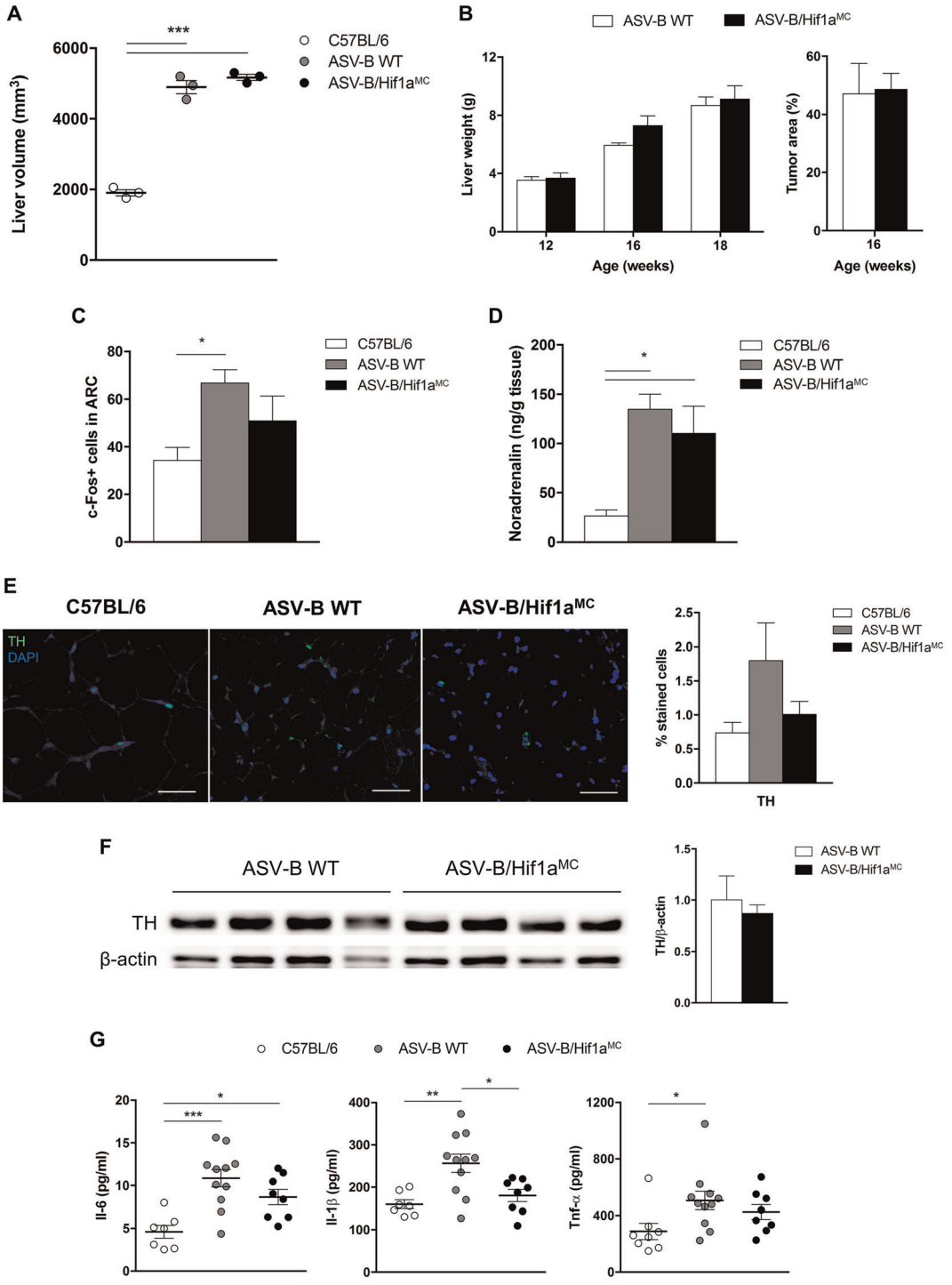



DOI: 10.1002/jcsm.12450

activated macrophages predominate under conditions of lipid mobilization,[38] we decided to analyse macrophage polarization in our model. We applied different experimental approaches, none of which showed a significant effect of *Hif1a* deletion on polarization of ATM (*Figure* 5A and 5B). Next, we determined ATM abundance via immunohistochemistry against F4/80. Interestingly, while a significant increase in ATM number was noted in ASV-B WT animals, this was completely inhibited upon *Hif1a* deletion (*Figure* 5C). Finally, we sought to address a possible contribution of ATM proliferation in our setting. As can be seen in *Figure* 5D, loss of *Hif1a* resulted in a significant decrease of Ki67-positive ATMs, arguing for a functional importance of HIF-1α for ATM proliferation that has not been previously appreciated.

### *Quantification of visceral adipose tissue in HCC patients*

The robust fat loss of ASV-B mice raised the question about the relevance of this phenotype for the human situation. To this end, we made use of a cohort of HCC patients ($n$ = 41; patient characteristics are given in Materials and methods section) without underlying liver cirrhosis as the ASV-B model is also not associated with hepatic fibrosis.[15] Interestingly, 34% of the patients indeed displayed low VAT as determined by the L3 VAT index (*Figure* 6). Low L3 VAT index was significantly associated with low body mass index ($P < 0.001$), young age ($P$ = 0.017), and female sex ($P$ = 0.027), while no association was found with tumour stage.

## Discussion

Clinical care of patients with HCC is characterized by various challenging obstacles. Co-morbidities of chronic liver disease, limited resectability due to cirrhosis-associated reduction of functional liver reserve, and the stout therapy resistance of HCC are among the most widely recognized impediments. For the longest time, the frailty and pronounced muscle weakness that characterizes the majority of HCC patients received much less attention. This has significantly changed in recent years as reports were published from independent groups about the important role of sarcopenia and cachexia in predicting both clinical course and response to therapy of HCC patients.[4,39–41] Cachexia is widely considered to be a multifactorial syndrome with various manifestations throughout the whole body. The causal pathogenesis of cachexia is very complex and involves a plethora of organs, cell types, hormones, cytokines/chemokines, growth factors, and inter-organ crosstalks.[42,43] To better understand the molecular and cell biological mechanisms that govern cachexia, model systems are needed that recapitulate the syndrome on a whole organism level.[44]

Here, we identify a robust cachexia phenotype in the well-established ASV-B mouse HCC model.[45] Various characteristic aspects of cachexia were noted in ASV-B mice, for example, loss of skeletal and heart muscle as well as adipose tissue mass over time, enhanced pro-inflammatory cytokine expression in blood, anaemia (*Figure* S4), and weight loss. While a number of animal models are available to study CAC,[46] only one is widely used with respect to HCC-associated CAC: the rat ascites hepatoma Yoshida AH-130 model.[47] This model proved of great value to test the anti-cachexia efficacy of various agents *in vivo*. However, it does not adequately mirror the pathogenesis of HCC as its heterotopic nature does not reflect the liver micro-environment. Furthermore, the AH-130 cells have been established more than 60 years ago,[48] and it is reasonable to assume that since then, they have acquired a lot of additional changes with unknown relevance for HCC pathogenesis. Recently, it was reported by the group of Erwin Wagner that 50% of mice harbouring di-ethyl-nitrosamine-induced HCCs developed signs of cachexia at 16–18 months of age.[29] While this is a very interesting finding that significantly expands the models available to study HCC-associated CAC, the long time spans in combination with a penetrance of 50% are surely obstacles against widespread use of this model. Against this background, it is important to note that in ASV-B mice, we were able to detect signs of cachexia with 100% penetrance as early as 12 weeks of age. We therefore consider the ASV-B model to be a powerful addition to the available methodology enabling a better understanding of the mechanistic underpinnings that underlie HCC-associated CAC.

Loss of adipose tissue is a well-known aspect of CAC and has been noted in animal models as well as samples from patients with various types of cancer.[49] It has been reported that adipose tissue loss precedes muscle wasting[50] and that inhibition of the former is able to slow down the latter.[14] Reduced peripheral fat content in CAC can be the result of three different processes in adipocytes: lipid uptake, intracellular *de novo* lipogenesis, and lipid release.[3] Our finding of VAT wasting in ASV-B mice is well in line with various other murine CAC models[49] and also with the rat hepatoma Yoshida AH-130 model.[11] To the best of our knowledge, we are the first to report a functional significance of macrophages for HCC-associated fat loss. Intercrosses of ASV-B with mice showing defective myeloid cell-mediated inflammation resulted in aggravated fat loss. Via immunohistochemistry, we could show greater macrophage abundance in adipose tissue from WT tumour-bearing mice, while this phenotype was completely inhibited in knockout mice. This led us to hypothesize that HCC-induced adipose tissue mobilization results in macrophage influx, ultimately inhibiting lipid release. This would be well in line with earlier reports showing macrophage-mediated suppression of lipid mobilization from

**Figure 5** Macrophage phenotype and proliferation in visceral adipose tissue. *(A)* (left) Representative images of F4/80 and Ym-1 immunofluorescence in epididymal white adipose tissue (eWAT) from ASV-B wild type (WT) ($n$ = 4) and Hif1a$^{MC}$ ($n$ = 5) mice, scale bars 50 μm; (right) quantification of F4/80/Ym-1 double staining, stained cells calculated as relative percentage to all counted cells. *(B)* mRNA expression analysis of markers for classically (*Tnfa*, *Nos2*, and *Cd274*) and alternatively (*Arg1*, *Mrc1*, *Clec10a*, and *Il-10*) activated macrophages in eWAT from 16 weeks old ASV-B WT ($n$ = 4) and Hif1a$^{MC}$ ($n$ = 5) mice. *(C)* (left) Representative images of immunofluorescence staining of F4/80 in eWAT from C57BL/6 ($n$ = 5), ASV-B WT ($n$ = 4), and ASV-B/Hif1a$^{MC}$ ($n$ = 5) mice, scale bars 50 μm; (right) quantification of staining, positive stained cells calculated as relative percentage of all counted cells. *(D)* (left) Representative images of immunofluorescence staining of F4/80 and Ki67 in eWAT from C57BL/6 ($n$ = 6), ASV-B WT ($n$ = 4), and ASV-B/Hif1a$^{MC}$ ($n$ = 5) mice, scale bars 50 μm; (right) quantification of staining, double positive stained cells calculated as relative percentage of all counted cells. Data show means with SEM. $^{*}P < 0.05$; $^{**}P < 0.01$ according to unpaired Student's $t$-test *(A, B)* and one-way analysis of variance followed by Tukey post hoc test *(C, D)*.

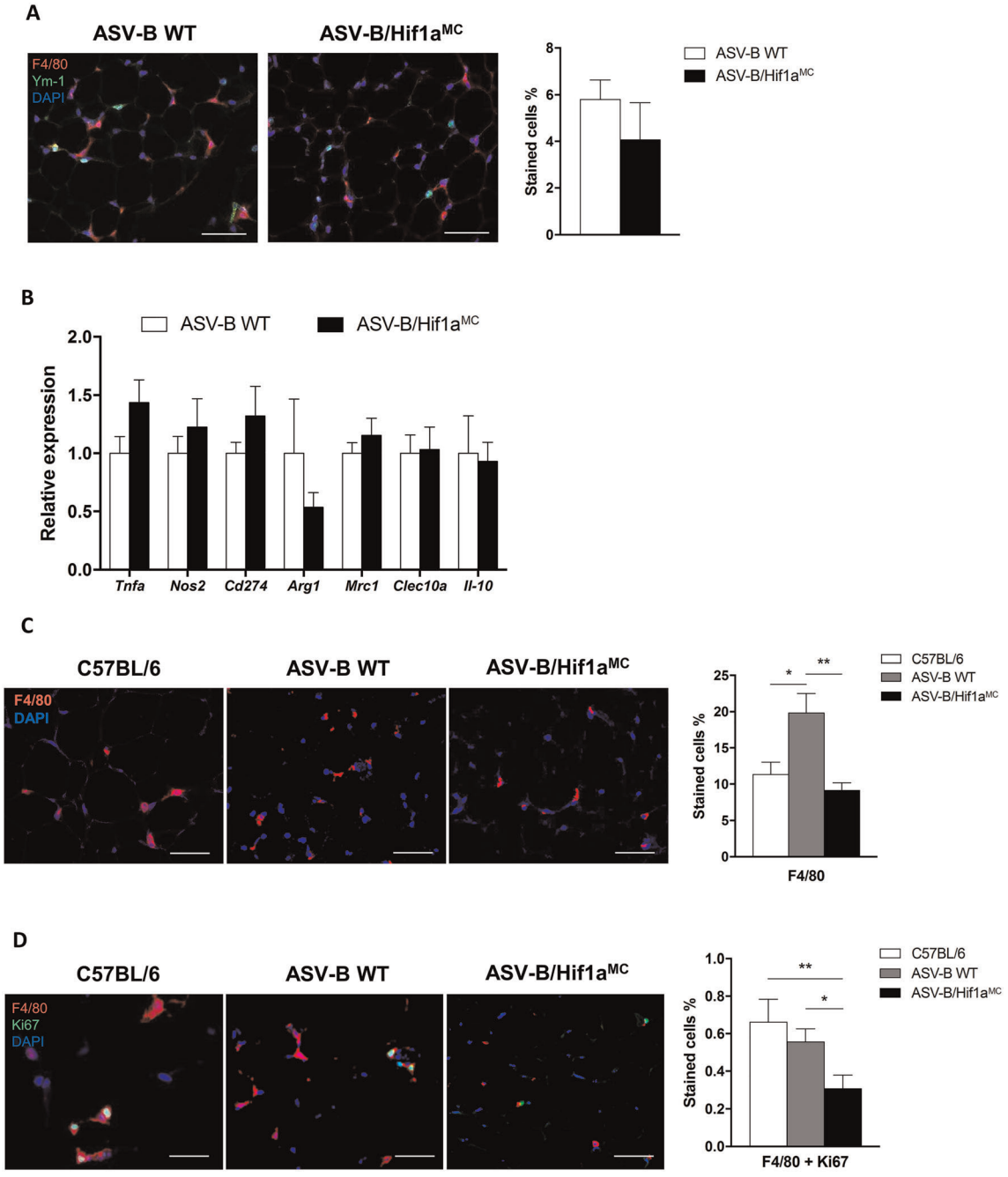



DOI: 10.1002/jcsm.12450

**Figure 6** A subgroup of human hepatocellular carcinoma (HCC) patients shows a reduced amount of visceral adipose tissue (VAT). Distribution of 41 patients according to L3 VAT index that was calculated from computed tomography images of patients. The patient group was divided into tertiles for L3 VAT index, and the lower tertile was compared with the medium/high tertile. The low tertile L3 VAT index was defined by a cut-off value of 35.

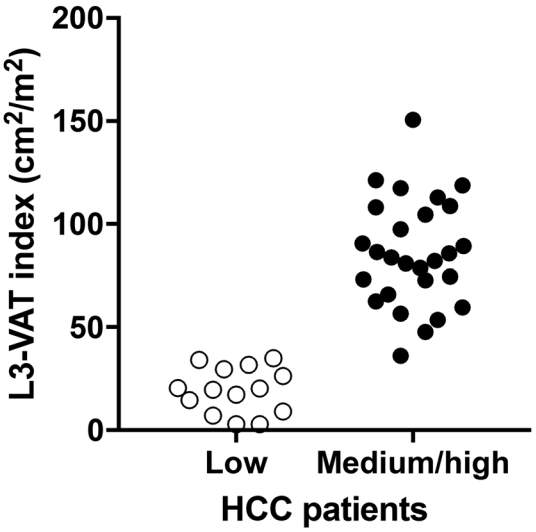


adipose tissue in response to fasting and pharmacologically induced lipid release in mice.[37] Greater macrophage numbers have also been reported in adipose tissue of patients with CAC,[51] underscoring the need to better understand the functional significance of these cells for cancer cachexia.

To analyse the role of macrophages for HCC-associated cachexia, we made use of a mouse model displaying a defect in myeloid cell-mediated inflammation.[26] This is achieved by conditional deletion of *Hif1a* in cells of late myeloid differentiation via the Cre/loxP system.[52] *Hif1a* encodes for the transcription factor hypoxia-inducible factor 1α (HIF-1α), the principle mediator of the cellular response to hypoxia.[53] HIF-1α target genes control virtually every aspect of the hypoxic response, for example, erythropoiesis, angiogenesis, glucose metabolism, and cell cycle modifications. Inactivation of *Hif1a* in myeloid cells severely impairs energy generation, leading to robustly compromised cellular function and defective myeloid cell-mediated inflammation.[26] Our finding of reduced macrophage abundance in adipose tissue during HCC-associated cachexia is well in line with earlier findings by us and others, demonstrating impaired chemotaxis and migration of *Hif1a*-deficient macrophages, neutrophils, and eosinophils in a wide range of underlying pathologies.[26,54] One limitation of our study is that we were not able to identify the origin of ATM. The pool of resident ATMs is composed of cells that developed from yolk sac-derived progenitors and from monocyte precursors, respectively.[55] To clearly differentiate between these, lineage tracing methodology has to be applied, which was out of the scope of the current project.

In addition, the important question as to the molecular stimuli that attract macrophages to adipose tissue in HCC-bearing mice remains to be addressed in the future. Published work points towards adipocyte-secreted chemokines, for example, MCP-1/CCL2, and free fatty acids.[37,56] Of note, expression of the MCP-1 receptor CCR2 on monocytes[57] and signal transduction induced by TLR4,[58] the putative cellular receptor for free fatty acids,[59] are strongly influenced by HIF-1α, potentially explaining the reduced macrophage abundance in adipose tissue upon *Hif1a* deletion. In addition to macrophage abundance, our results show reduced proliferation of ATM in conditional *Hif1a* knockout mice. While local proliferation of macrophages has been shown in adipose tissue inflammation associated with obesity,[60] we are the first to report local macrophage proliferation in the setting of CAC-associated fat loss. Furthermore, a functional role of HIF-1α for macrophage proliferation has thus far only been reported for bovine macrophages after infection with the parasite *Theileria annulata*[61] and not for murine cells. Admittedly, the percentage of local macrophages that proliferate is rather small. Hence, the functional significance of this observation for CAC-induced lipolysis remains elusive and needs to be validated in future studies. In recent years, hypoxia and hypoxia-associated pathways, for example, tissue vascularization, emerged as important aspects of various adipose tissue pathologies, most prominently obesity-associated inflammation.[62] The intriguing question whether adipose tissue hypoxia is of functional relevance for lipolysis in ASV-B mice was out of the scope of the current project and is currently being investigated by us.

In line with the mouse model data, we were able to show that a subgroup of HCC patients displays a reduced amount of VAT. This strongly suggests that HCC is also capable of inducing fat mobilization from peripheral stores in human patients. To prove this convincingly, one would have to perform longitudinal patient studies, that is, analysing the same patient at different stages of disease progression, a venture out of scope of the current project. In other cancer types, for example, pancreatic adenocarcinoma, adipose tissue loss is a well-known phenomenon with clinical relevance as it is able to predict survival.[63] The functional importance of adipose tissue loss for the clinical course of HCC needs to be addressed by future studies with larger patient cohorts. In light of the leading role of adipose tissue loss for the sequence of events characterizing cancer cachexia,[14] a better understanding of the mechanisms driving HCC-associated fat mobilization is warranted.

## Acknowledgements

Research in the Cramer lab was supported by the Deutsche Forschungsgemeinschaft (CR 133/2-1 until 2-4). We also

gratefully acknowledge the support by the European Research Council to T.L. [ERC-StG NeoNano (309495) and ERC-PoC CONQUEST and PIcelles (680882, 813086)]. We are indebted to Dr Maaike Oosterveer (Department of Pediatrics and Laboratory Medicine, University Medical Center Groningen, The Netherlands) for help with the *ex vivo* lipolysis assay. We are grateful to Dr Thomas Ritz (University Hospital Aachen) and Prof. Dr Thomas Longerich (University of Heidelberg) for help with multispectral immunofluorescence imaging. We thank Mrs Constance Hobusch for excellent technical support. The authors certify that they comply with the ethical guidelines for publishing in the *Journal of Cachexia, Sarcopenia and Muscle*.[64]

## Online supplementary material

Additional supporting information may be found online in the Supporting Information section at the end of the article.

**Figure S1.** Relative expression of *Hif1a* mRNA in bone marrow-derived macrophages isolated from WT and Hif1a$^{MC}$ mice to evaluate the knockout efficiency.

**Figure S2.** Measurements of skeletal muscle (GC, TA, EDL, soleus) and heart muscle were performed at 12 (right, 12w) and 16 (left, 16w) weeks of age. Data show means with SEM and were analyzed by unpaired Student's *t*-test.

**Figure S3.** Adipocyte cell area analysis was performed using Adiposoft software as described in Figure 3A and materials and methods. This scatter plot represents the distribution of all adipocytes according to their size together with the mean of each group.

**Figure S4.** Blood work of ASV-B mice. Complete blood counts in C57BL/6 ($n$ = 5) and ASV-B ($n$ = 6) mice at 16 weeks of age were performed in an automated analyzer. WBC: White blood cells, RBC: Red blood cells, HGB: Hemoglobin, HCT: Hematocrit, MCV: Mean corpuscular volume, MCH: Mean corpuscular hemoglobin, MCHC: Mean corpuscular hemoglobin concentration, PLT: Platelets. Data represent means with SEM analyzed by unpaired Student's *t*-test; *$P < 0.05$; **$P < 0.01$; *** $P < 0.001$.

## Conflict of interest

None declared.

## References

1. Evans WJ, Morley JE, Argiles J, Bales C, Baracos V, Guttridge D, et al. Cachexia: a new definition. *Clin Nutr (Edinburgh, Scotland)* 2008;**27**:793–799.
2. Fearon K, Arends J, Baracos V. Understanding the mechanisms and treatment options in cancer cachexia. *Nat Rev Clin Oncol* 2013;**10**:90–99.
3. Argiles JM, Busquets S, Stemmler B, Lopez-Soriano FJ. Cancer cachexia: understanding the molecular basis. *Nat Rev Cancer* 2014;**14**:754–762.
4. Chang KV, Chen JD, Wu WT, Huang KC, Hsu CT, Han DS. Association between loss of skeletal muscle mass and mortality and tumor recurrence in hepatocellular carcinoma: a systematic review and meta-analysis. *Liver cancer* 2018;**7**:90–103.
5. Meza-Junco J, Montano-Loza AJ, Baracos VE, Prado CM, Bain VG, Beaumont C, et al. Sarcopenia as a prognostic index of nutritional status in concurrent cirrhosis and hepatocellular carcinoma. *J Clin Gastroenterol* 2013;**47**:861–870.
6. Dodson RM, Firoozmand A, Hyder O, Tacher V, Cosgrove DP, Bhagat N, et al. Impact of sarcopenia on outcomes following intra-arterial therapy of hepatic malignancies. *J Gastrointest Surg* 2013;**17**:2123–2132.
7. Kaido T, Ogawa K, Fujimoto Y, Ogura Y, Hata K, Ito T, et al. Impact of sarcopenia on survival in patients undergoing living donor liver transplantation. *Am J Transplant Off J Am Soc Transplant Am Soc Transplant Surg* 2013;**13**:1549–1556.
8. Mir O, Coriat R, Blanchet B, Durand JP, Boudou-Rouquette P, Michels J, et al. Sarcopenia predicts early dose-limiting toxicities and pharmacokinetics of sorafenib in patients with hepatocellular carcinoma. *PLoS ONE* 2012;**7**:e37563.
9. DeBoer MD. Animal models of anorexia and cachexia. *Expert Opin Drug Discovery* 2009;**4**:1145–1155.
10. Tessitore L, Bonelli G, Baccino FM. Early development of protein metabolic perturbations in the liver and skeletal muscle of tumour-bearing rats. A model system for cancer cachexia. *Biochem J* 1987;**241**:153–159.
11. Carbo N, Costelli P, Tessitore L, Bagby GJ, Lopez-Soriano FJ, Baccino FM, et al. Anti-tumour necrosis factor-α treatment interferes with changes in lipid metabolism in a tumour cachexia model. *Clin Sci (London, England: 1979)* 1994;**87**:349–355.
12. Palus S, von Haehling S, Flach VC, Tschirner A, Doehner W, Anker SD, et al. Simvastatin reduces wasting and improves cardiac function as well as outcome in experimental cancer cachexia. *Int J Cardiol* 2013;**168**:3412–3418.
13. Springer J, Tschirner A, Haghikia A, von Haehling S, Lal H, Grzesiak A, et al. Prevention of liver cancer cachexia-induced cardiac wasting and heart failure. *Eur Heart J* 2014;**35**:932–941.
14. Das SK, Eder S, Schauer S, Diwoky C, Temmel H, Guertl B, et al. Adipose triglyceride lipase contributes to cancer-associated cachexia. *Science (New York, NY)* 2011;**333**:233–238.
15. Dubois N, Bennoun M, Allemand I, Molina T, Grimber G, Daudet-Monsac M, et al. Time-course development of differentiated hepatocarcinoma and lung metastasis in transgenic mice. *J Hepatol* 1991;**13**:227–239.
16. Gremse F, Stark M, Ehling J, Menzel JR, Lammers T, Kiessling F. Imalytics preclinical: interactive analysis of biomedical volume data. *Theranostics* 2016;**6**:328–341.
17. Nguyen KD, Qiu YF, Cui XJ, Goh YPS, Mwangi J, David T, et al. Alternatively activated macrophages produce catecholamines to sustain adaptive thermogenesis. *Nature* 2011;**480**:104–U272.
18. Kir S, White JP, Kleiner S, Kazak L, Cohen P, Baracos VE, et al. Tumour-derived PTH-related protein triggers adipose tissue browning and cancer cachexia. *Nature* 2014;**513**:100–104.
19. Bustin SA, Benes V, Garson JA, Hellemans J, Huggett J, Kubista M, et al. The MIQE guidelines: minimum information for publication of quantitative real-time PCR experiments. *Clin Chem* 2009;**55**:611–622.
20. Adamsky A, Kol A, Kreisel T, Doron A, Ozeri-Engelhard N, Melcer T, et al. Astrocytic activation generates de novo neuronal potentiation and memory enhancement. *Cell* 2018;**174**:59–71.e14.
21. Mourtzakis M, Prado CM, Lieffers JR, Reiman T, McCargar LJ, Baracos VE. A practical and precise approach to quantification

of body composition in cancer patients using computed tomography images acquired during routine care. *Appl Physiol Nutr Metab = Physiologie appliquee, nutrition et metabolisme* 2008;**33**:997–1006.
22. Williams BAM, Mandrekar SJ, Cha SS, Furth A. Finding optimal cutpoints for continuous covariates with binary and time-to-event outcomes. *Technical Report Series* 2006;**79**.
23. Dupuy E, Hainaud P, Villemain A, Bodevin-Phedre E, Brouland JP, Briand P, et al. Tumoral angiogenesis and tissue factor expression during hepatocellular carcinoma progression in a transgenic mouse model. *J Hepatol* 2003;**38**:793–802.
24. Tsoli M, Robertson G. Cancer cachexia: malignant inflammation, tumorkines, and metabolic mayhem. *Trends Endocrinol Metab* 2013;**24**:174–183.
25. Caronni N, Savino B, Bonecchi R. Myeloid cells in cancer-related inflammation. *Immunobiology* 2015;**220**:249–253.
26. Cramer T, Yamanishi Y, Clausen BE, Forster I, Pawlinski R, Mackman N, et al. HIF-1α is essential for myeloid cell-mediated inflammation. *Cell* 2003;**112**:645–657.
27. Ryden M, Agustsson T, Laurencikiene J, Britton T, Sjolin E, Isaksson B, et al. Lipolysis—not inflammation, cell death, or lipogenesis—is involved in adipose tissue loss in cancer cachexia. *Cancer* 2008;**113**:1695–1704.
28. Dahlman I, Mejhert N, Linder K, Agustsson T, Mutch DM, Kulyte A, et al. Adipose tissue pathways involved in weight loss of cancer cachexia. *Br J Cancer* 2010;**102**:1541–1548.
29. Petruzzelli M, Schweiger M, Schreiber R, Campos-Olivas R, Tsoli M, Allen J, et al. A switch from white to brown fat increases energy expenditure in cancer-associated cachexia. *Cell Metab* 2014;**20**:433–447.
30. Rohwer N, Jumpertz S, Erdem M, Egners A, Warzecha KT, Fragoulis A*, et al*. Non-canonical HIF-1 stabilization is essential for intestinal tumorigenesis. bioRxiv 2018.
31. Nogueiras R, Wiedmer P, Perez-Tilve D, Veyrat-Durebex C, Keogh JM, Sutton GM, et al. The central melanocortin system directly controls peripheral lipid metabolism. *J Clin Invest* 2007;**117**:3475–3488.
32. Koch M, Varela L, Kim JG, Kim JD, Hernandez-Nuno F, Simonds SE, et al. Hypothalamic POMC neurons promote cannabinoid-induced feeding. *Nature* 2015;**519**:45–50.
33. Seoane-Collazo P, Ferno J, Gonzalez F, Dieguez C, Leis R, Nogueiras R, et al. Hypothalamic-autonomic control of energy homeostasis. *Endocrine* 2015;**50**:276–291.
34. Fischer K, Ruiz HH, Jhun K, Finan B, Oberlin DJ, van der Heide V, et al. Alternatively activated macrophages do not synthesize catecholamines or contribute to adipose tissue adaptive thermogenesis. *Nat Med* 2017;**23**:623–630.
35. Faber J, Vos P, Kegler D, van Norren K, Argiles JM, Laviano A, et al. Beneficial immune modulatory effects of a specific nutritional combination in a murine model for cancer cachexia. *Br J Cancer* 2008;**99**:2029–2036.
36. Argiles JM, Stemmler B. The potential of ghrelin in the treatment of cancer cachexia. *Expert Opin Biol Ther* 2013;**13**:67–76.
37. Kosteli A, Sugaru E, Haemmerle G, Martin JF, Lei J, Zechner R, et al. Weight loss and lipolysis promote a dynamic immune response in murine adipose tissue. *J Clin Invest* 2010;**120**:3466–3479.
38. Olefsky JM, Glass CK. Macrophages, inflammation, and insulin resistance. *Annu Rev Physiol* 2010;**72**:219–246.
39. Iritani S, Imai K, Takai K, Hanai T, Ideta T, Miyazaki T, et al. Skeletal muscle depletion is an independent prognostic factor for hepatocellular carcinoma. *J Gastroenterol* 2015;**50**:323–332.
40. Fujiwara N, Nakagawa H, Kudo Y, Tateishi R, Taguri M, Watadani T, et al. Sarcopenia, intramuscular fat deposition, and visceral adiposity independently predict the outcomes of hepatocellular carcinoma. *J Hepatol* 2015;**63**:131–140.
41. Kroh A, Uschner D, Lodewick T, Eickhoff RM, Schoning W, Ulmer FT*, et al*. Impact of body composition on survival and morbidity after liver resection in hepatocellular carcinoma patients. Hepatobiliary & pancreatic diseases international: HBPD INT 2018.
42. Fearon KC, Glass DJ, Guttridge DC. Cancer cachexia: mediators, signaling, and metabolic pathways. *Cell Metab* 2012;**16**: 153–166.
43. Petruzzelli M, Wagner EF. Mechanisms of metabolic dysfunction in cancer-associated cachexia. *Genes Dev* 2016;**30**:489–501.
44. Ballaro R, Costelli P, Penna F. Animal models for cancer cachexia. *Curr Opin Support Palliat Care* 2016;**10**:281–287.
45. Daskalow K, Rohwer N, Raskopf E, Dupuy E, Kuhl A, Loddenkemper C, et al. Role of hypoxia-inducible transcription factor 1α for progression and chemosensitivity of murine hepatocellular carcinoma. *J Mol Med (Berlin, Germany)* 2010;**88**:817–827.
46. Bennani-Baiti N, Walsh D. Animal models of the cancer anorexia-cachexia syndrome. *Support Care Cancer* 2011;**19**:1451–1463.
47. Pain VM, Randall DP, Garlick PJ. Protein synthesis in liver and skeletal muscle of mice bearing an ascites tumor. *Cancer Res* 1984;**44**:1054–1057.
48. Yoshida T. Contributions of the ascites hepatoma to the concept of malignancy of cancer. *Ann N Y Acad Sci* 1956;**63**:852–881.
49. Bing C, Trayhurn P. New insights into adipose tissue atrophy in cancer cachexia. *Proc Nutr Soc* 2009;**68**:385–392.
50. Agustsson T, Ryden M, Hoffstedt J, van Harmelen V, Dicker A, Laurencikiene J, et al. Mechanism of increased lipolysis in cancer cachexia. *Cancer Res* 2007;**67**: 5531–5537.
51. Batista ML Jr, Henriques FS, Neves RX, Olivan MR, Matos-Neto EM, Alcantara PS, et al. Cachexia-associated adipose tissue morphological rearrangement in gastrointestinal cancer patients. *J Cachexia Sarcopenia Muscle* 2016;**7**:37–47.
52. Clausen BE, Burkhardt C, Reith W, Renkawitz R, Forster I. Conditional gene targeting in macrophages and granulocytes using LysMcre mice. *Transgenic Res* 1999;**8**:265–277.
53. Palazon A, Goldrath AW, Nizet V, Johnson RS. HIF transcription factors, inflammation, and immunity. *Immunity* 2014;**41**:518–528.
54. Crotty Alexander LE, Akong-Moore K, Feldstein S, Johansson P, Nguyen A, McEachern EK, et al. Myeloid cell HIF-1α regulates asthma airway resistance and eosinophil function. *J Mol Med (Berlin, Germany)* 2013;**91**:637–644.
55. Röszer T. Understanding the biology of self-renewing macrophages. *Cell* 2018;**7**:103.
56. Ohira H, Fujioka Y, Katagiri C, Mamoto R, Aoyama-Ishikawa M, Amako K, et al. Butyrate attenuates inflammation and lipolysis generated by the interaction of adipocytes and macrophages. *J Atheroscler Thromb* 2013;**20**:425–442.
57. Dong F, Khalil M, Kiedrowski M, O'Connor C, Petrovic E, Zhou X, et al. Critical role for leukocyte hypoxia inducible factor-1α expression in post-myocardial infarction left ventricular remodeling. *Circ Res* 2010;**106**:601–610.
58. Frede S, Stockmann C, Freitag P, Fandrey J. Bacterial lipopolysaccharide induces HIF-1 activation in human monocytes via p44/42 MAPK and NF-κB. *Biochem J* 2006;**396**:517–527.
59. Shi H, Kokoeva MV, Inouye K, Tzameli I, Yin H, Flier JS. TLR4 links innate immunity and fatty acid-induced insulin resistance. *J Clin Invest* 2006;**116**:3015–3025.
60. Amano SU, Cohen JL, Vangala P, Tencerova M, Nicoloro SM, Yawe JC, et al. Local proliferation of macrophages contributes to obesity-associated adipose tissue inflammation. *Cell Metab* 2014;**19**:162–171.
61. Metheni M, Lombes A, Bouillaud F, Batteux F, Langsley G. HIF-1α induction, proliferation and glycolysis of Theileria-infected leukocytes. *Cell Microbiol* 2015;**17**:467–472.
62. Rasouli N. Adipose tissue hypoxia and insulin resistanceJournal of investigative medicine: the official publication of the American Federation for. *Clin Res* 2016;**64**:830–832.
63. Di Sebastiano KM, Yang L, Zbuk K, Wong RK, Chow T, Koff D, et al. Accelerated muscle and adipose tissue loss may predict survival in pancreatic cancer patients: the relationship with diabetes and anaemia. *Br J Nutr* 2013;**109**:302–312.
64. von Haehling S, Morley JE, Coats AJS, Anker SD. Ethical guidelines for publishing in the Journal of Cachexia, Sarcopenia and Muscle: update 2017. *J Cachexia Sarcopenia Muscle* 2017;**8**: 1081–1083.